NOTES AND CORRESPONDENCE

Error Characteristics of the Atmospheric Correction Algorithms Used in Retrieval of Sea Surface Temperatures from Infrared Satellite Measurements: Global and Regional Aspects

AJOY KUMAR, PETER J. MINNETT, GUILLERMO PODESTÁ, AND ROBERT H. EVANS

Meteorology and Physical Oceanography Division, Rosenstiel School of Marine and Atmospheric Science, University of Miami, Miami, Florida

19 September 2001 and 18 June 2002

ABSTRACT

A database of cotemporal, collocated satellite and in situ observations is used to examine the association between the brightness temperature differences measured by the thermal infrared channels (T45) of the Advanced Very High Resolution Radiometer (AVHRR) and water vapor estimates (ω) derived from the Special Sensor Microwave Imager (SSM/I). This channel difference is used to estimate the atmospheric correction (due mostly to water vapor absorption) in sea surface temperature (SST) algorithms. The association between T45 and ω is found to be greatest for tropical latitudes; for mid- and high latitudes, the association is best during summer. However, the association tends to decrease toward mid- and higher latitudes during other periods. SST residual errors (satellite − buoy) show a negative mean in the Tropics, suggesting undercorrection for water vapor attenuation in the Tropics. This underestimation is explicitly shown for SST residuals in the high-water-vapor regimes of the Arabian Sea. In mid- and high latitudes, the variability of atmospheric water vapor and air–sea temperature difference contributes to the weaker association between T45 and ω and results in positive mean SST residual errors. A differential form of SST algorithm that incorporates the use of a ''first-guess estimate'' that correlates with SST is observed to give the least residual error.

1. Introduction

Sea surface temperature (SST) is an important parameter in the exchange of energy and gases between the ocean and the atmosphere. It is emerging as the primary focus in understanding the amount and rate of future warming and associated climate changes. Satellite-derived SST maps are routinely obtained and are extensively used for climate and weather forecasting applications (e.g., May et al. 1998; Walton et al. 1998). The increase in importance of global, synoptic SST maps has resulted in the need for accurate temperature fields.

Infrared (IR) measurements of SST from satellites are made in spectral regions at which the atmosphere is relatively transparent and at which the surface emission is measurable to adequate accuracy. In reality, this limits the measurements to the 3.7–4.2- and 10–12-μm spectral regions. Because of the susceptibility to contamination of the surface emission by reflected solar radiation during the sunlit part of each orbit in the shorter wavelength interval, the mainstay of satellite SST determination has been based on measurements in the 10–12-μm interval. Surface emission in this part of the spectrum is large, because it is close to the peak of the Planck function at typical temperatures of the sea surface. Within this spectral interval the atmospheric absorption is dominated by the effects of water vapor (Saunders and Edwards 1989).

The mean distribution of water vapor in the atmosphere shows a maximum in the equatorial region, with a seasonal migration in the summer hemisphere, and a gradual decrease to polar latitude (Peixoto and Oort, 1991). The annual-mean distribution of specific humidity near the surface is about 18 g kg^{-1} in the equatorial regions and decreases to about 1 g kg^{-1} or less over the polar regions. In general, the specific humidity decreases with height and latitude. More than 90% of water vapor is confined to the layer below 500 hPa. The steepest gradients and most pronounced temporal variability of water vapor is in the subtropics. The spatial variability shows a maximum around 20°N, with a large difference between the winter and summer values. These maxima are related to the large amounts of water vapor over the

Corresponding author address: Ajoy Kumar, Meteorology and Physical Oceanography Division, Rosenstiel School of Marine and Atmospheric Science, University of Miami, Miami, FL 33149.
E-mail: akumar@rsmas.miami.edu

western borders of the subtropical highs during summer and over the Asian monsoon area.

Several methods have been proposed to correct for the atmospheric attenuation of the surface signal (Hagan 1989; Wick et al. 1992; Emery et al. 1994; Schluessel et al. 1990; Barton 1995; Walton et al. 1998). Most algorithms to measure SST are based on the hypothesis that the total attenuation in one channel can be determined from the measured brightness temperature difference between any two channels (e.g., McMillin 1975; Barton 1995). For the Advanced Very High Resolution Radiometers (AVHRR), this means the difference in top-of-atmosphere brightness temperatures measured in channel 4 (T_4) and channel 5 (T_5), denoted here as T45. Since water vapor is the main cause of the temperature deficit (T_4 − SST; T_5 − SST), this assumes that the effect of the water vapor can be represented as a function of the brightness temperature difference (McMillin 1975). As pointed out by Barton (1995), all sea surface temperature algorithms have this basic theoretical dependence on the differential absorption technique.

The simplest form of the differential absorption SST algorithm is the multichannel SST (MCSST):

$$\text{MCSST} = a + bT_4 + \gamma(T_4 - T_5), \quad (1)$$

where T_4 and T_5 are the brightness temperatures in AVHRR channels 4 and 5 and a and b are constants (McClain et al. 1985). The ''differential absorption'' term γ is defined as

$$\gamma = \frac{1 - \tau_4}{\tau_4 - \tau_5},$$

where τ is the transmittance through the atmosphere from the surface to the satellite in AVHRR channels 4 and 5. In cases of weak absorption, the transmittance can be approximated by $(1 - ku)$, where k is the mass absorption coefficient of the atmospheric absorbers and u is the pathlength (Barton 1995). In the MCSST algorithm, γ is assumed to be a constant. In a more advanced SST algorithm, called the cross-product SST (CPSST), γ is a function of channel brightness temperatures (Walton et al. 1998). Later, a simplified form of CPSST, the nonlinear SST (NLSST), was developed in which a scaled estimate of the surface temperature is used as γ (Walton et al. 1998):

$$\text{NLSST} = a + bT_4 + c(T_4 - T_5)\text{SST}_g + d(T_4 - T_5)[\sec(\theta) - 1], \quad (2)$$

where SST_g is a first-guess SST, θ is the satellite zenith angle measured at the sea surface and a, b, c, and d are coefficients derived by regression analysis against buoy SST. Note that the values of a, b, c, and d are different for each form of the atmospheric correction equation. Recently, another form of NLSST, the Pathfinder SST (PFSST), was developed with time-dependent coefficients estimated for two separate atmospheric regimes defined by T45 (Kilpatrick et al. 2001). The first-guess SST field, in this case, is a 1° interpolated global SST field (Reynolds and Smith 1994).

The coefficients in atmospheric correction algorithms are determined by regression of either collocated satellite and in situ measurements, mainly from buoys (e.g., Kilpatrick et al. 2001), or of numerical simulations of satellite measurements derived by radiative transfer modeling of the propagation of the infrared signal from the sea surface through a set of atmospheric conditions (e.g., Llewellyn-Jones et al. 1984; Minnett 1990; Zavody et al. 1995).

Another form of differential absorption algorithm is the quadratic SST (QSST):

$$\text{QSST} = a + bT_4 + c(T_4 - T_5) + d(T_4 - T_5)^2, \quad (3)$$

where the atmospheric moisture content can be estimated from the difference between channels 4 and 5 and added as a square to the linear correction (McMillin 1975). Emery et al. (1994) used water vapor fields (ω) derived from the Special Sensor Microwave Imager (SSM/I) in their water vapor SST (WVSST) algorithm:

$$\text{WVSST} = a + bT_4 + c(T_4 - T_5) + dW(T_4 - T_5), \quad (4)$$

where $W = W_o/\cos(\theta)$, W_o is the total column atmospheric water vapor from the sea surface to the satellite, and θ is the satellite zenith angle.

Despite the importance of atmospheric water vapor in defining the correction needed to determine accurate SSTs from satellites, there have been few successful attempts to document the association between water vapor and AVHRR radiances. In this paper, we analyze the spatial and temporal association between atmospheric water vapor content and AVHRR channel difference and explore its effect on SST estimates. Insight gained on the nature of these associations will allow us to better understand the performance of existing SST algorithms and to improve the parameterization of various terms in such algorithms.

Data from several sources were used in this study. Collocated, cotemporal AVHRR data and in situ measurements were obtained from the multiyear, multisatellite Pathfinder Matchup Database (PMDB), developed as part of the AVHRR Oceans Pathfinder program (information was available online at the time of writing at http://www.rsmas.miami.edu/groups/rrsl/pathfinder/Matchups/). The details of the PMDB, Pathfinder algorithm, and coefficient determination are discussed in Kilpatrick et al. (2001). The PMDB are assembled over a broad geographic and temporal distribution, so that algorithm performance can be studied over a wide range of atmospheric and oceanic regimes.

Cloud contamination is one of the major sources of error in satellite-derived SST retrievals. A sequence of tests is used to remove cloud-contaminated matchups and large errors caused by other factors, prior to coefficient estimation. Although the data used here have passed these tests, a few matchups persist that have large residuals. To minimize errors from the outliers, we have

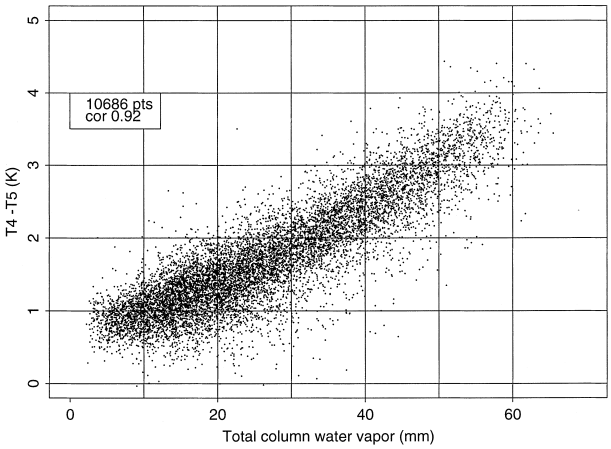

FIG. 1. Scatter diagram showing the relationship between channel difference and SSM/I-derived water vapor fields. The data legends indicate the number of satellite–buoy matchups for 1997.

excluded matchups with absolute values of residuals >2 K. However, because of the relatively good performance of various tests, very few extreme values (less than 2%) were excluded with the ±2.0 K criteria, and it should not significantly influence our results. The analysis was carried out using matchups for 1997, which had the most extensive geographic distribution of all years available. Our analysis is based on 19 912 global matchups.

Estimates of integrated atmospheric columnar water vapor ω in the PMDB were derived from the SSM/I (Wentz 1997). The water vapor retrieval algorithm has a stated rms accuracy of ±1 mm. For this study, we first made daily 0.5° latitude–longitude grid maps that combine the SSM/I 0.25° day and night gridded data. Water vapor at the locations of the in situ–AVHRR matchups were spatially interpolated from the gridded daily water vapor file.

2. Association between AVHRR channel difference and water vapor

A key factor in achieving an accurate satellite-derived SST retrieval is the temporal and spatial relationship between atmospheric water vapor and the measured AVHRR channel difference. In Fig. 1, the association between ω and T45 is shown for 1997. The figure suggests an almost linear relationship. In general, the two quantities seem to be associated throughout the range of observed ω. Although the correlation is high ($\rho >$ 0.9, where ρ is correlation coefficient), it is accompanied by a large spread [standard deviation (SD) = 0.93 K] of T45 values for a given ω. Since the matchups represent a wide variety of atmospheric conditions, the above association appears to suggest temporal and spatial variation exist between T45 and ω.

To understand the spatial and temporal association between ω and T45, we divided the matchups into six latitudinal regions consisting of tropical (0°–20° latitude), midlatitude (20°–40°), and high-latitude (40°–60°) bands for each hemisphere. We further divided the matchups into four seasons, each consisting of a 3-month period, starting with January of 1997. We then calculated the mean, median, SD of SST residuals, and ρ between the T45 and water vapor in each of these spatial and temporal subsets to examine the linear association between these variables. The robust correlation coefficient is defined as

$$\rho = \frac{E(X - \mu_1)(Y - \mu_2)}{\sigma_1 \sigma_2}, \tag{5}$$

where μ_1 and μ_2 are the means and σ_1 and σ_2 are the standard deviations. The robust confidence intervals of the population correlation coefficient at the 95% level are computed. Since the plots are similar for both hemispheres, only the Northern Hemisphere results are presented in Figs. 2a–f. Histograms of SST residuals are also shown.

The Tropics exhibit a strong year-round association between T45 and ω ($\rho > 0.9$; Fig. 2a). The histograms of PFSST residuals (Pathfinder SST − buoy SST), however, always show a negative mode in this region (Fig. 2b). This result clearly suggests that, although T45 is correlated well with ω in the Tropics, the PFSST algorithm undercorrects in regions of high atmospheric water vapor.

In contrast to the Tropics, the mid- and high latitudes show a progressively weaker association between T45 and ω (see Figs. 2c,e). Such latitudinal changes in association are not clearly visible when the data are grouped together as in Fig. 1. The correlation ($\rho \sim 0.7$–0.5) decreases from midlatitudes poleward. Similarly, the mean of the PFSST residuals tends to get more positive from midlatitudes poleward (Figs. 2d,f).

The largest annual variations in water vapor occur in relatively low latitudes over the oceans. These latitudinal shifts in water vapor likely influence the association between T45 and ω. During warmer periods for the Northern Hemisphere (April–September), the T45 values are generally correlated with ω, associated with the higher proportion of water vapor during this season. During other periods, especially at midlatitudes, the relation between T45 and ω shows maximum spread.

Because of orbit precession and scanning pattern, the AVHRR will view spots on the earth at different angles. One consequence of the varying viewing geometry is that a higher satellite zenith angle will result in a longer atmospheric path, which, in turn, will result in higher atmospheric absorption of surface-emitted radiance and changes in the amount of radiance emitted by the atmosphere. Another effect associated with viewing geometry is the change on surface emissivity (Masuda et al. 1988). For these reasons, we investigated the effect of satellite zenith angle on the previously described association between T45 and ω.

Figure 3a shows nonparametric trend lines (Cleveland

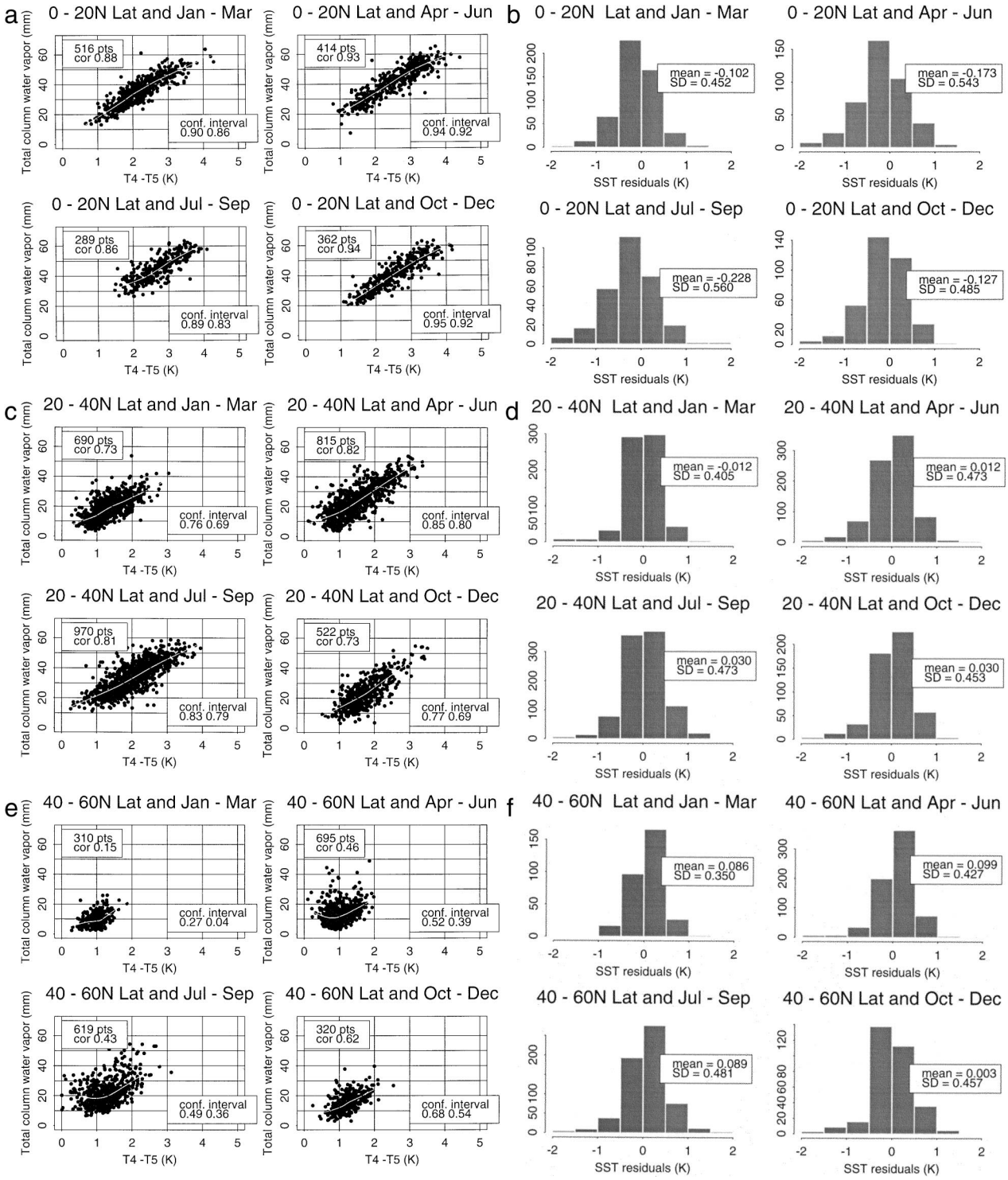

FIG. 2. (a) Scatter diagrams showing the relationship between channel difference and SSM/I-derived water vapor fields for matchups in latitudes (a) 0°–20°N, (c) 20°–40°N, and (e) 40°–60°N. The matchups are further divided into four quarters to show seasonal variations. Histograms of the temperature difference between PFSST and in situ buoy SST for (b) 0°–20°N, (d) 20°–40°N, and (f) 40°–60°N. The data legends indicate the mean of the residuals and the SD.

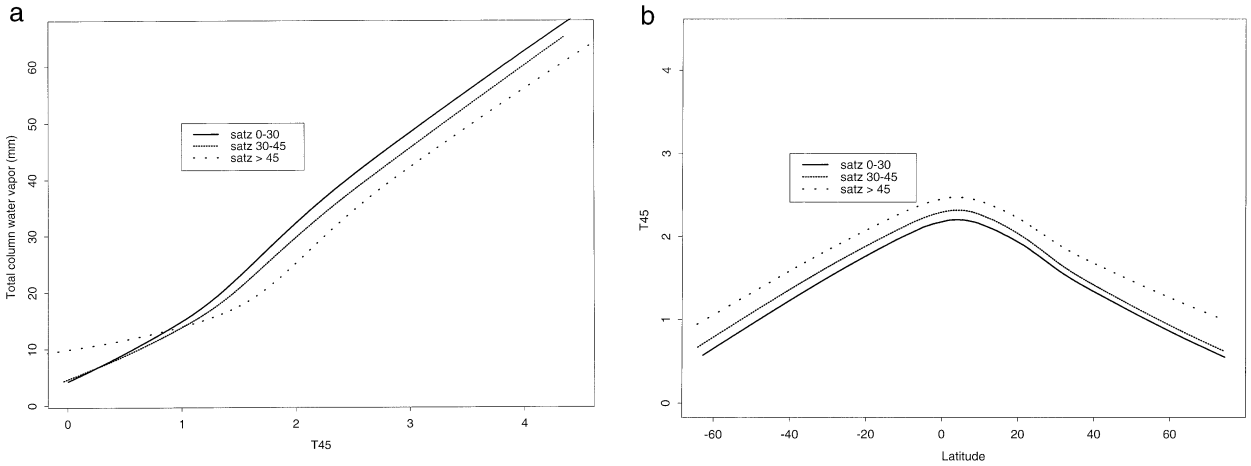

FIG. 3. (a) The association of T45 with ω shown using nonparametric trend lines (Cleveland et al. 1988). (b) The association of T45 with latitude shown using nonparametric trend lines (Cleveland et al. 1988). The legends indicate trend lines encompassing satellite zenith angles 0°–30°, 30°–45°, and greater than 45°.

et al. 1988) for T45 versus ω fitted for different satellite zenith angles. The trend lines encompassing satellite zenith angles less than 45° are not very different from one another. However, the trend lines for satellite zenith angle greater than 45° shows that, at lower ω, the T45 values are higher than corresponding values fitted for small zenith angles. As ω increases, the trend becomes similar to those of other curves, suggesting a multiplicative effect among satellite zenith angle, T45, and ω.

In Fig. 3b, the trend lines for T45 is plotted versus latitude for different satellite zenith angles. As satellite zenith angle increases, the T45 difference should increase as a result of the increased pathlength, approximately proportional to sec(θ). The T45 difference near the equator (mostly in summer) is nearly independent of satellite zenith angle. This effect must be compensated by an increased contribution by the zenith angle term in SST algorithms. The high-zenith-angle case near the poles is influenced in a different manner. Here, the larger differences between the curves are due to effects of surface emissivity with zenith angle and increased proportion of surface radiance reaching the satellite.

a. Temperature deficit variation in the association between T45 and ω

At high environmental temperatures, frequently associated with high water vapor, the satellite-derived SSTs are usually underpredicted. This effect becomes more severe as viewing angle increases. To understand how the interaction of oceanic and atmospheric conditions affects SST retrievals, we analyze the association among the temperature deficit term TD (TD4 = SST − T_4; TD5 = SST − T_5), T45, and ω. The temperature deficit indicates the amount of correction that an algorithm must provide to account for atmospheric effects.

Because most of the atmospheric effects on infrared radiance can be ascribed to atmospheric water vapor, we examine the association between TD4 and TD5 with ω. Figure 4a shows TD4 and TD5 increase with ω and that the association is not linear. This result is expected, but it was unexpected that the spread of the association would be largely uniform throughout the observed water vapor range (~1°C). At about 20 mm, the envelope of points does start to show a slight increase. The change in the slope is due to the fact that, at low ω, SST, T_4, and T_5 increase as a function of ω. Below ω of about 20 mm, T_4 and T_5 respond closely to changes in SST; therefore, the difference between the two quantities (TD4 and TD5) increases slowly with increasing ω. As ω gets higher, SST usually keeps increasing, but the corresponding T_4 and T_5 values do not increase as much. As a consequence, the difference between TD4 and TD5 grows more rapidly as ω increases. There is a steeper slope for TD5 than for TD4 because of greater absorption at the longer-wavelength channel 5. As observed in the case of TD and ω, there is a similar, nonlinear relationship between TD and T45 (Fig. 4b). In the envelope of points described by TD4 and TD5 with T45, one can also observe a change in the slope at around 30 mm.

It is apparent in Fig. 4b that the scatter of the association between TD and T45 is much lower than in the case of TD versus ω (Fig. 4a). Much of the scatter could be due to uncertainty in the SSM/I-derived ωs resulting from instrument noise, algorithmic error, or data compositing (Barton 1995). A more fundamental reason for T45 being more closely related to TD than ω is that the TD values for a given ω may show significant differences because of variability in the vertical distribution of temperature and moisture (Eyre 1987). The T45 value carries implicit information about the vertical distribution of water vapor and temperature in the atmosphere, whereas the SSM/I water vapor estimate is an

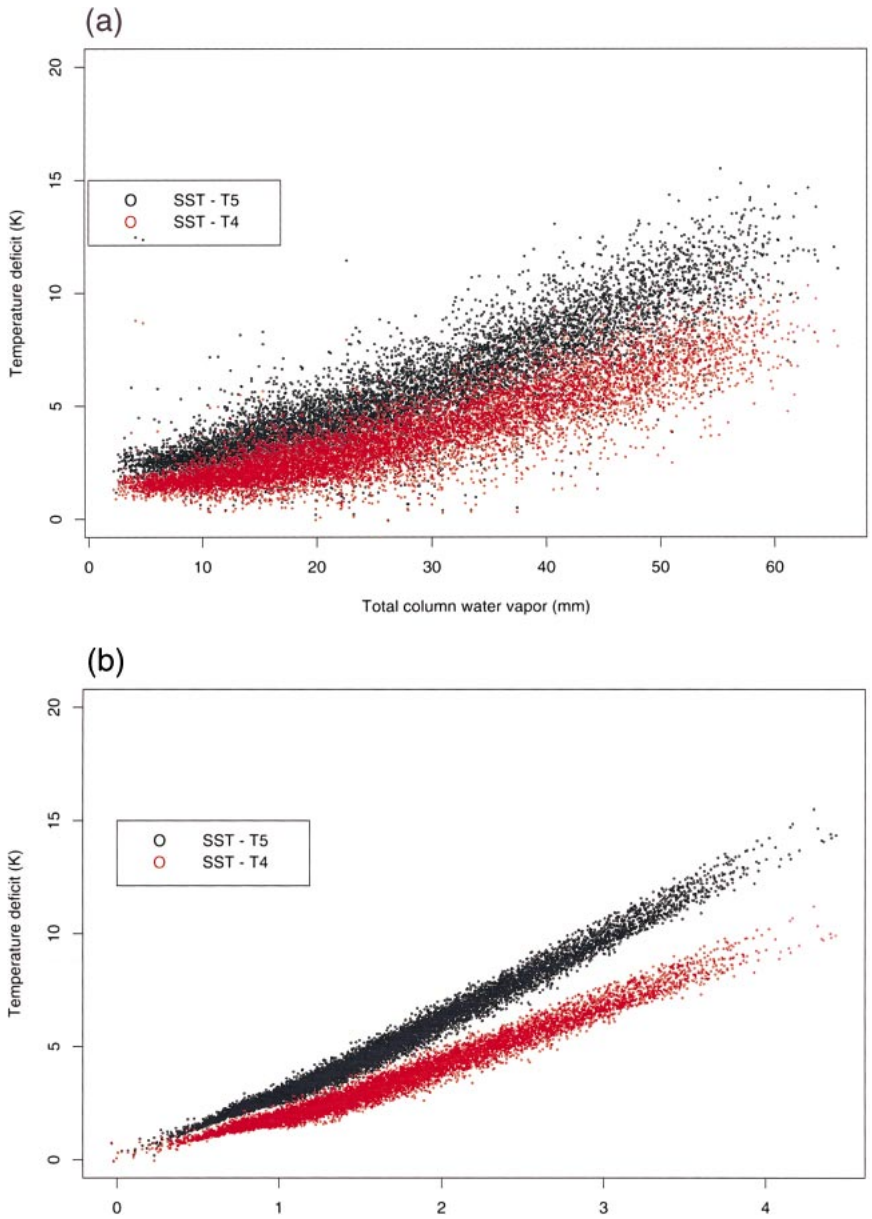

FIG. 4. (a) Scatterplot of SSM/I-derived water vapor with temperature deficit term. (b) Scatterplot of T45 values with temperature deficit term. Data legends indicate the temperature deficit with channel 4 and channel 5.

integrated columnar value. Furthermore, T45 responds to absorbers and emitters other than water vapor (Minnett 1986; R. Evans and G. Podestá 1996, unpublished manuscript).

As the fraction of ground radiance (signal of interest) in the top-of-atmosphere measurement decreases with water vapor and viewing angle, the signal-to-noise ratio of the atmospheric correction problem decreases. Any deviations from the usual distribution of atmospheric conditions (to which algorithms are optimized) may introduce proportionally higher variability in high-water-vapor regimes. In the above analysis, the variability for a given T45 value is as much as 1°C, which may explain the noticeable increase in the variability of satellite-derived SST residuals in high-SST (high ω) regions.

b. High-water-vapor conditions: The Arabian Sea

To quantify the error in the estimation of satellite-derived SST at high-water-vapor regions, we have used data from the Arabian Sea. The Arabian Sea, with its monsoon-driven atmospheric circulation, is a region of high seasonal atmospheric water vapor. The Joint Global Ocean Flux Study in situ SST data, obtained from the

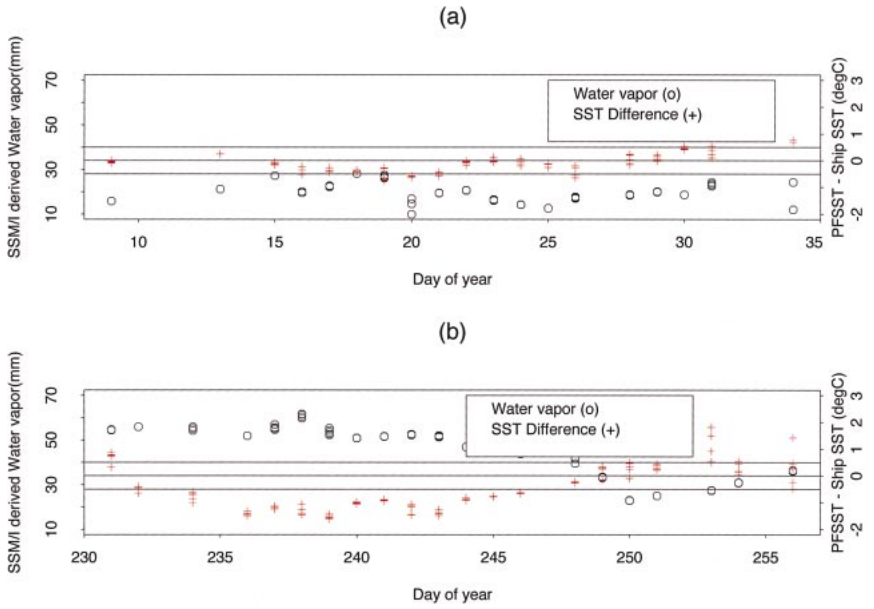

FIG. 5. Scatterplot showing the water vapor concentration and SST residual variation for the two periods, (a) dry and (b) moist, in the Arabian Sea. The SST residual in this case is the difference between Pathfinder SST and temperature from ship-based thermosalinograph data.

project's archives (available at the time of writing online at http://www1.whoi.edu/jg/dir/jgofs/) are used in this analysis.

The seasonal behavior of ω and SST residual in the Arabian Sea is shown in Fig. 5. During parts of the year when ω is less than approximately 30 mm (Fig. 5a), SST residuals are small. In contrast, during periods when ω is greater than approximately 40 mm (Fig. 5b), a large negative bias of SST residuals is observed. This result suggests that, at a precipitable water vapor value greater than approximately 40 mm, the PFSST undercorrects. In Fig. 6, the T45 values corresponding to the period in Fig. 5 are shown; during periods when ω is greater than about 40 mm, T45 values do not increase proportionate to ω (Fig. 6b). Hence, the T45 increase is not sufficient to correct entirely for the temperature

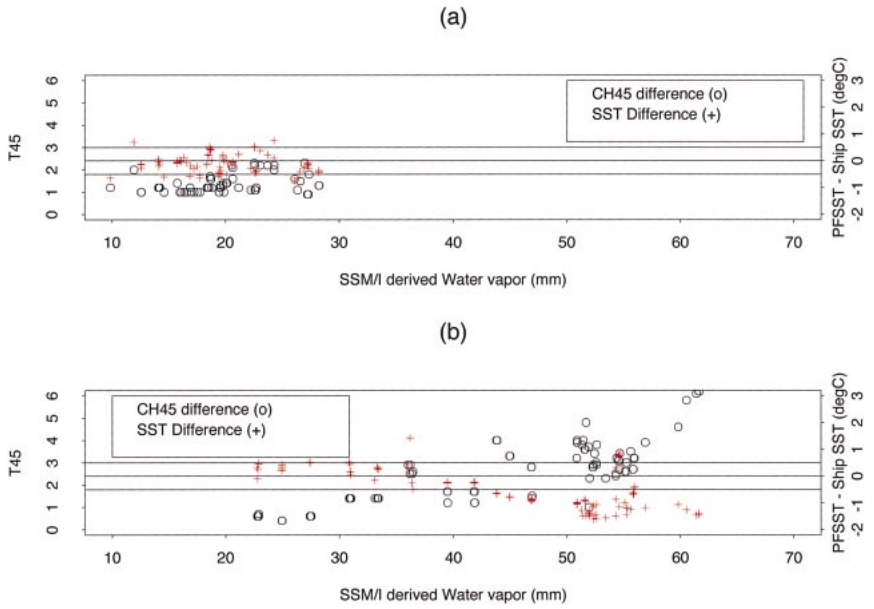

FIG. 6. Scatterplot showing the T45 and SST residual variation for the two periods, (a) dry and (b) moist, in the Arabian Sea. The SST residual in this case is the difference between Pathfinder SST and temperature from ship-based thermosalinograph data.

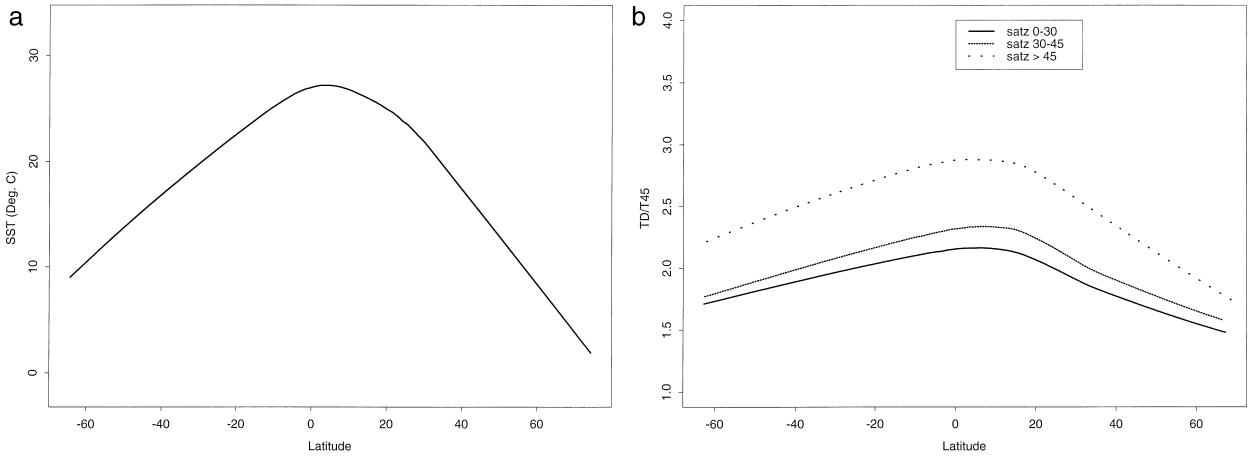

FIG. 7. (a) The association of (a) satellite-derived SST from PMDB and (b) TD/T45 with latitude, shown using nonparametric trend lines (Cleveland et al. 1988). The legends indicate trend lines encompassing satellite zenith angles 0°–30°, 30°–45°, and greater than 45°.

deficit caused by atmospheric absorption of radiances. However, in Fig. 1, for the global distribution it is seen that T45 values still respond to ω in high-water-vapor regimes, probably related to the large scatter in the data points, as discussed above, which masks regional behavior.

c. *Zonal variability in the association between T45 and ω*

What is the cause behind the decrease of (T45) sensitivity to ω at mid-and high latitudes? One reason may be related to the variations in the frequency distribution of ω within each latitudinal band. That is, if there is a higher proportion of low ω in a latitudinal band, it is likely that the association between T45 and ω will be lower. Another reason may be related to the vertical distribution of temperature and moisture associated with baroclinic perturbations along the polar front.

Let us consider a simple differential absorption SST algorithm that can be described in terms of T45 and TD as

$$(\mathrm{SST} - T_4) = \kappa(T_4 - T_5), \tag{6}$$

where κ is some function of atmospheric property that correlates with SST in the NLSST and PFSST algorithms. If the use of a surface temperature value as a T45 coefficient weighting term were correct, then the latitudinal dependence of SST derived with the Pathfinder algorithm (Fig. 7a) would be proportional to the ratio of the temperature deficit (TD4) and T45 (Fig. 7b). However, the ratio shows a varying behavior that is not exactly proportional to derived SST. The shape of the latitudinal mean SST profiles differs from the T45 coefficient, suggesting a tendency to overweight the atmospheric correction at midlatitudes relative to the Tropics. This may explain how the mean of SST residuals at mid- and high latitudes is positive. Investigating this latter aspect is beyond the scope of this work and will be undertaken in a future study.

3. SST algorithm performance

We evaluated the performance of three alternative formulations of SST algorithms: 1) PFSST, 2) QSST [as suggested in Barton (1995)], and 3) WVSST (Emery et al. 1994). The form of each algorithm is given above [Eqs. (2), (3), and (4)].

The global matchups were first divided randomly into two groups. The first group is used to estimate coefficients for each algorithm. These coefficients are then used on the second (withheld, or validation) group to estimate SSTs. As a case study, coefficients and SSTs are also calculated separately for the Arabian Sea region. For all three algorithms, in situ buoy SSTs are used to estimate the residuals.

The performance of the global algorithms show better behavior of PFSST and WVSST residuals when compared with QSST (Fig. 7a). However, the PFSST algorithm has the lowest rms (0.541 K) and mean (−0.019 K). In contrast to PFSST and WVSST, the global QSST residuals are biased toward the positive direction, which suggests that an approach that incorporates an independent factor (such as ω or ''first-guess SST'') along with T45 in correcting for temperature deficit may give better results. Histograms of Arabian Sea SST residuals also show similar behavior to that of global algorithms (Fig. 8a).

To further test the various algorithms, we estimated coefficients and SSTs for three different latitudinal groups: the tropical (0°–20°N), midlatitude (20°–40°N), and high-latitude (40°–60°N). In all latitudinal bands, the PFSST algorithm has the least rms and shows the best behavior of residuals (Fig. 8b). In comparison, the WVSST has slightly higher rms in the Tropics and midlatitudes, but the behavior of residuals is biased, espe-

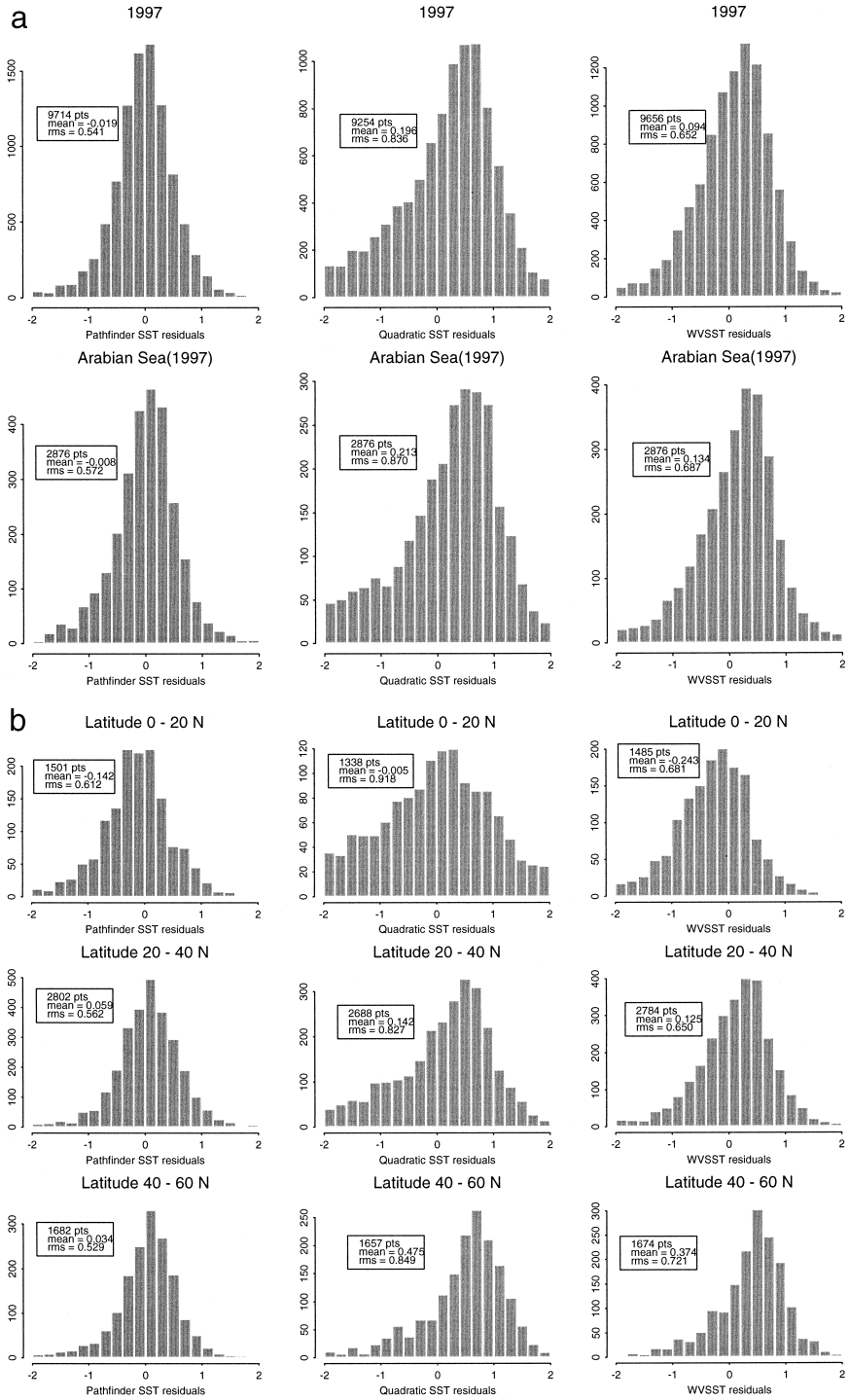

FIG. 8. (a) Histogram of SST residuals using Pathfinder, quadratic, and WVSST algorithms. The SST residuals are computed as the difference between satellite and in situ buoy measurements. The data legends indicate the number of matchups, the mean, and the rms of the SST residuals. The top half of (a) shows residuals using matchups for 1997. The bottom half shows residuals using matchups for the Arabian Sea region only. (b) Same as in (a), but for different latitudes (all plots).

cially at high latitudes. The QSST algorithm, with its squared T45 term, gives the largest rms of SST residuals.

4. Discussion and conclusions

The overall theme of this paper is the investigation of associations between atmospheric water vapor and infrared radiation measured by spaceborne infrared radiometers, such as the AVHRR, used in SST estimation. Since water vapor is the main absorber of infrared radiation in the atmospheric windows used for satellite remote sensing of SST, it is important to understand how it affects the radiances received by the spacecraft radiometer and, consequently, its influence on the performance of various alternative SST algorithms.

The analysis showed that spatial and temporal differences in the association between T45 and ω exist. We have demonstrated a statistically significant association between T45 and ω in the Tropics (0°–20°N), which is consistent with the traditional assumption that the T45 difference is related to atmospheric moisture. However, the statistical significance decreases for mid- (20°–40°N) and high (40°–60°N) latitudes. Also, the strongest association between T45 and ω exists seasonally during the summer months, when higher-water-vapor conditions are likely. Our analyses tend to agree with those of Minnett (1986) and Emery et al. (1994), in that the T45 temperature difference is not a strong function of water vapor for midlatitudes and high latitudes.

The mean of SST residuals (Pathfinder SST − buoy SST) tends to be negative in the Tropics, which suggests that under high-atmospheric-water-vapor conditions, T45, which is used as a proxy to estimate the amount of atmospheric correction needed in SST algorithms, does not increase linearly with ω. T45 estimates tend to undercorrect in the presence of high atmospheric moisture. An undercorrection by T45 in such regimes has been suggested by Walton et al. (1998) and is demonstrated here for the high-water-vapor regions of the Arabian Sea. Our analysis showed that, at $\omega >$ about 40 mm, T45 values are slightly smaller than what they should be, which leads to inadequate correction in SST algorithms and increased uncertainty in SST residuals.

The association of TD with both T45 and ω can be described by a piecewise linear fit with a break in the slope at about 1 K. The reason for the increase in slope is unclear but is possibly related to fundamental differences in the nature of moisture and temperature profiles between high-latitude (low ω) and low-latitude (high ω) environments (R. Evans and G. Podestá 1996, unpublished manuscript). The scatter of points increases with TD, showing that, at high ω, a significant amount of the sensed radiation originates from the atmosphere rather than the sea surface. Although the emission of atmospheric radiation is closely correlated with the absorption of ground radiance, there are subtle changes in the spectral composition of the total radiance sensed that may affect the T45 difference and thus the SST retrievals.

This work also showed that the association between T45 and ω is influenced by satellite zenith angle. The variation of T45 at different satellite zenith angles near the equator is small, suggesting the influence of high ω as described above. At satellite zenith angles of 45° and greater, this analysis showed greater uncertainties of T45 values, which may introduce significant errors in SST retrievals. This result indicates that the $[\sec(\theta) - 1]$ term in the atmospheric correction algorithms does not fully represent the effects of changing pathlengths across the swath.

We have evaluated the performance of three SST algorithms with in situ buoys taken as the standard reference to estimate the SST residual. Our analyses demonstrate that the three different correction schemes yield different results. The QSST has the greatest rms and largest variation in SST residuals for all latitudes, which may be directly related to the amplification of uncertainties in T45 by the squared term. The scatter in Fig. 4b indicates some basic accuracy limit for QSST-type algorithms. For a given T45 value, the temperature deficit varies by nearly a degree. This is probably the reason why WVSST and PFSST perform better, since, in these algorithms, a variable gamma parameter is used.

Our results suggest that integrated atmospheric columnar water vapor estimates do contribute to the atmospheric correction problem. In general, the WVSST performs well except at high latitudes, at which water vapor absorption is minimum and other gases and surface emissivity complicate the correction needed. The scatter in ω (Fig. 4a) may be due to SSM/I retrieval errors. One reason WVSST does well despite the large scatter in ω may be because random errors cancel each other.

However, in the absence of data on vertical distribution of temperature and moisture, the T45 values are the only variables that carry information on these quantities in SST algorithms. This reason may be why PFSST behaves better than WVSST. A first-guess SST estimate appears to reduce the biases in T45 values that are discussed above. We have shown that the SST term in PFSST tends to overweight the atmospheric correction at midlatitudes. This overcorrection may also contribute to the positive mean of SST residuals at midlatitudes. Walton et al. (1998) have demonstrated the relative insensitivity of the NLSST algorithm to errors in the climatological temperature used as the first-guess SST.

The regression coefficients in these alternate SST algorithms reflect the mean state of the atmosphere and ocean for the in situ measurements used in their derivation. As a consequence, application of these algorithms to situations removed from these mean conditions will lead to a loss of accuracy (Eyre 1987; Minnett 1986, 1990; Shenoi 1999). In an earlier work, Kumar et al. (2000) analyzed the suitability of a global PFSST al-

gorithm for various regional atmospheric and oceanic conditions and found that a larger geographical distribution of points (representing a wide variety of atmospheric and oceanic conditions) used to estimate the coefficients produced better SST retrievals. In a recent study, Emery et al. (2001) also have shown that the number of in situ observations is less important than their geographic distribution.

To further improve satellite SST estimates, an accurate description of the mean atmospheric conditions relevant to infrared remote sensing, classified by region and season or airmass type is needed (Minnett 1986, 1991). Satellite sensors that provide synoptic information on atmospheric structure may provide new opportunities to improve satellite-derived SST retrievals.

Acknowledgments. The authors thank Kay Kilpatrick for her assistance with the Pathfinder Matchup Database. We also thank two anonymous reviewers for excellent reviews and suggestions. This work is supported by NASA Grant NAG 56577.

REFERENCES

Barton, I. J., 1995: Satellite-derived sea surface temperatures: Current status. *J. Geophys. Res.,* **100,** 8777–8790.

Cleveland, W. S., S. J. Devlin, and E. Grosse, 1988: Regression by local fitting: Methods, properties and computational algorithm. *J. Econometrics,* **37,** 87–114.

Emery, W. J., Y. Yu, G. A. Wick, P. Schluessel, and R. W. Reynolds, 1994: Correcting infrared satellite estimates of sea surface temperature for atmospheric water vapor attenuation. *J. Geophys. Res.,* **99,** 5219–5236.

——, D. J. Baldwin, P. Schluessel, and R. W. Reynolds, 2001: Accuracy of in situ sea surface temperature used to calibrate infrared satellite measurements. *J. Geophys. Res.,* **106,** 2387–2405.

Eyre, J. R., 1987: On systematic errors in satellite sounding products and their climatological mean values. *Quart. J. Roy. Meteor. Soc.,* **113,** 279–292.

Hagan, D. E., 1989: A basic limitation of the split window method for SST retrievals when applied to a wide range of water vapor conditions. *Geophys. Res. Lett.,* **16,** 815–817.

Kilpatrick, K., G. Podestá, and R. Evans, 2001: Overview of the NOAA/NASA Pathfinder version 4.2 algorithm for sea surface temperature and associated matchup database. *J. Geophys. Res.,* **106,** 815–817.

Kumar, A., P. J. Minnett, G. Podestá, and R. Evans, 2000: Analysis of Pathfinder SST algorithm for global and regional conditions. *Proc. Indian Acad. Sci., Earth Planet. Sci.,* **109,** 395–405.

Llewellyn-Jones, D. T., P. J. Minnett, R. W. Saunders, and A. M. Zavody, 1984: Satellite multichannel infrared measurements of sea surface temperature of the N. E. Atlantic Ocean using AVHRR/2. *Quart. J. Roy. Meteor. Soc.,* **110,** 613–631.

Masuda, K., T. Takashima, and Y. Takayama, 1998: Emissivity of pure and sea waters for the model sea surface in the infrared window regions. *Remote Sens. Environ.,* **24,** 313–329.

May, D. A., M. M. Parmeter, D. S. Olszewski, and B. D. McKenzie, 1998: Operational processing of satellite sea surface temperature retrievals at the Naval Oceanographic Office. *Bull. Amer. Meteor. Soc.,* **79,** 397–407.

McClain, E. P., W. G. Pichel, and C. C. Walton, 1985. Comparative performance of AVHRR-based multichannel sea surface temperatures. *J. Geophys. Res.,* **90,** 11 587–11 601.

McMillin, L. M., 1975: Estimation of sea surface temperatures from two infrared window measurements with different absorption. *J. Geophys. Res.,* **80,** 5113–5117.

Minnett, P. J., 1986: A numerical study of the effects of anomalous North Atlantic atmospheric conditions on the infrared measurement of sea surface temperature from space. *J. Geophys. Res.,* **91,** 8509–8521.

——, 1990: The regional optimization of infrared measurements of sea surface temperature from space. *J. Geophys. Res.,* **95,** 13 497–13 510.

——, 1991: Consequences of sea surface temperature variability on the validation and applications of satellite measurements. *J. Geophys. Res.,* **96,** 18 475–18 489.

Peixoto, J. P., and A. H. Oort, 1991: *Physics of Climate.* Amer. Inst. Phys., 520 pp.

Reynolds, R. W., and T. M. Smith, 1994: Improved global sea surface temperature analyses using optimum interpolation. *J. Climate,* **7,** 929–948.

Saunders, R., and D. P. Edwards, 1989: Atmospheric transmittances for the AVHRR channels. *Appl. Opt.,* **28,** 4154–4160.

Schluessel, P., W. Emery, H. Grassl, and T. Mammen, 1990: On the bulk-skin temperature difference and its impact on satellite remote sensing of sea surface temperature. *J. Geophys. Res.,* **95,** 13 341–13 356.

Shenoi, S. C., 1999: On the suitability of global algorithms for the retrieval of SST from the north Indian Ocean using NOAA/AVHRR data. *Int. J. Remote Sens.,* **20,** 11–29.

Walton, C. C., W. G. Pichel, J. F. Sapper, and D. A. May, 1998: The development and operational application of nonlinear algorithms for the measurement of sea surface temperatures with the NOAA polar-orbiting environmental satellites. *J. Geophys. Res.,* **103,** 27 999–28 012.

Wentz, F. J., 1997: A well-calibrated ocean algorithm for SSM/I. *J. Geophys. Res.,* **102,** 8703–8718.

Wick, G. A., W. J. Emery, and P. Schluessel, 1992: A comprehensive comparison between satellite measured skin and multichannel sea surface temperature. *J. Geophys. Res.,* **97,** 5569–5595.

Zavody, A. M., C. T. Mutlow, and D. T. Llewellyn-Jones, 1995: A radiative transfer model for sea-surface temperature retrieval for the Along Track Scanning Radiometer. *J. Geophys. Res.,* **100,** 937–952.